Food Chemistry 363 (2021) 130245

Contents lists available at ScienceDirect

Food Chemistry

journal homepage: www.elsevier.com/locate/foodchem

Fabrication of label-free and ultrasensitive electrochemical immunosensor based on molybdenum disulfide nanoparticles modified disposable ITO: An analytical platform for antibiotic detection in food samples

Amit K. Yadav [a], Damini Verma [a,b], G.B.V.S. Lakshmi [a], Sergei Eremin [c,d], Pratima R. Solanki [a,*]

[a] Special Centre for Nanoscience, Jawaharlal Nehru University, New Delhi 110067, India
[b] Amity Institute of Applied Science, Amity University, Noida, U.P. 201313, India
[c] Department of Chemical Enzymology, M.V.Lomonosov Moscow State University, Moscow, Russia
[d] A.N. Bach Institute of Biochemistry, Research Center of Biotechnology of the Russian Academy of Sciences, Moscow, Russia

ARTICLE INFO

Keywords:
Antibiotics
Ampicillin
Differential pulse voltammetry
Electrochemical immunosensor
Molybdenum disulfide
Nanoparticles

ABSTRACT

Here, we aimed to fabricate a label-free immunosensing platform for the first time based on molybdenum disulfide nanoparticles ($nMoS_2NPs$) deposited on ITO) coated glass substrate for the electrochemical detection of ampicillin (AMP). The stable and high surface area of $nMoS_2NPs$ were made by a low-temperature one-step hydrothermal route, bestowing the carrying capacity of anti-AMP (antibody against AMP) through an amide linkage. The spectroscopic, morphological, and structural characterization of the proposed electrodes were performed using various analytical and electrochemical techniques. The differential pulse voltammetry technique was utilized to evaluate anti-AMP and AMP interaction on the electrode surface. The developed immunosensor exhibits high sensitivity, a broad detection range having a significant detection limit towards detection of AMP having excellent selectivity, acceptable stability, and reproducibility. Furthermore, the applicability of the proposed immunosensor was tested in spiked milk, water, and orange juice, and the results confirmed the consistency of the immunosensor.

1. Introduction

The World Health Organization (WHO) has been reported that antimicrobial-resistant (AMR) bacteria have become the basic risk to human health caused due to declining potency and excessive use of antibiotics (Michael, Dominey-Howes, & Labbate, 2014). During clinical/veterinary practice, antibiotics have selective pressure on bacteria that speeds up the bacterial development having AMR properties owing to pharmaceutical accumulation in the water systems and food chains. The annual mortality rate related to infections from antibiotic-resistant bacteria is as much as nearly 23,000 deaths in the U.S., according to a report of the Centers for Disease Control and Prevention (Syska, 2013). Recent studies have revealed that antibiotics with enormous concentrations are found in India's drinking water, surpassing the maximum regulatory limits (MRLs). This has led to a severe effect on susceptible residents existing close to industrial services, as nearly 58,000 newborns dies in these areas of India from multi-drug resistant infections (Hall, 2018). The tetracyclines, sulfonamides, macrolides, fluoroquinolones, and β-lactams classes of antibiotic compounds are often present in aquatic environments. Ampicillin (AMP) [Fig. S1] is one of the most commonly used β-lactam antibiotics, a water-soluble chemical substance. It is extensively used in agriculture, livestock, poultry, aquaculture, veterinary, and human medicine to prevent and treat contagious diseases (Wang et al., 2019) due to the remarkable destroying ability for gram-negative and positive bacteria. The overdose of antibiotics or antibiotic residues can cause severe environmental and food safety concerns that triggered various human and animal health complications in past decades involving endocarditis, membranitis, intestinal infection, and irritability (Wang et al., 2019). Therefore, detecting AMP residues in foodstuffs is essential for protecting human health as it can lead to adverse reactions, comprising anaphylactic disorders. Hence, there is an urgent need to develop reliable, sensitive, portable, inexpensive, and fast detection methods for detecting AMP, specifically.

Numerous commercial diagnostic tests are currently available for antibiotics in food samples and environments, either unable to detect

* Corresponding author.
E-mail addresses: partima@mail.jnu.ac.in, pratimarsolanki@gmail.com (P.R. Solanki).

https://doi.org/10.1016/j.foodchem.2021.130245
Received 13 February 2021; Received in revised form 14 May 2021; Accepted 27 May 2021
Available online 29 May 2021

antibiotic compounds selectively or need a lengthy response time (several hours) and offer semi-quantitative information only (Jamieson et al., 2020). Over the decades, several attempts have been tried for developing various effective techniques for the detection of AMP residues in waters and agricultural products, which includes Raman spectroscopy, high-performance liquid chromatography (HPLC), liquid chromatography-mass spectrometry/ mass spectrometry (HPLC-MS/MS), surface plasmon resonance (SPR), spectrophotometry, colorimetric methods, electrochemiluminescence, enzyme-linked immunosorbent assay (ELISA), nuclear magnetic resonance, and immunochemical detection (Yuan, Yan, Shaga, & He, 2021). Such methods are sensitive to AMP detection, but due to high cost, sophisticated instrumentation, complicated sample preparation, and complex instrument operation, it restricts its practical applications for the on-site assays. Therefore, simple, rapid, miniaturized, and low-cost electrochemical immunosensor hold considerable attention for detecting antibiotics (Cardoso, Tavares, & Sales, 2018). Further, it not only combines the principles of immunological analysis for detecting the target analytes electrochemically but also offers the benefits of specificity and high selectivity. In this context, by combining the high selectivity of antibodies with the highly sensitive transducers, antibodies-based sensors, i.e., immunosensors, have become an effective analytical technique for antibiotic residues determination (Fowler, Wong, Halsall, & Heineman, 2008). Also, antibody usage enhances the efficiency of the immunochemical response due to faster assay kinetics along with an increased surface area and also minimizes matrix effect with improved washing and separation steps (Solé, Merkoci, & Alegret, 2001).

The modification of working electrodes with highly active material is necessity to develop high-performance electrochemical immunosensors. Recently, broad attention has been given to grow 2D nanomaterials, in particular, the transition metal dichalcogenides (TMDCs) such as tungsten diselenide (WSe_2) and molybdenum disulfide (MoS_2) due to their favored graphene-like layer structure (Zhang, Zhang, Su, & Wei, 2015). As a typical TMDCs, MoS_2 is a layered nanomaterial composed of covalently bound S-Mo-S layers in which each Mo is coordinated to six S atoms through weak *van der Waals force* of attractions (Zhu et al., 2013), thus improving the planar electric transportation properties. MoS_2 has been widely researched by an increasing number of scientists for their use in biosensors owing to its distinct chemical and physical properties like robust electron transfers ability/high electrocatalytic activity, exceptional biocompatibility, easy modification and functionalization (Huang et al., 2014), semiconducting properties, and large surface area which enhances the adsorption of target molecules (Zhou, Lou, & Xie, 2013). It has a large junction and high surface-to-volume ratio (Yan, Shi, Sui, Deng, & Gao, 2017) of the electrode/electrolyte with good chemical stability, which are desirable properties for electrochemical biosensors. To get the full advantages of MoS_2 having a high surface area, nanostructured MoS_2 nanoparticles ($nMoS_2$ NPs) have been made recently and used to fabricate a few sensors and biosensors (Kim, Mondal, Min, & Choi, 2018). Shin*et al.,* fabricated a biosensor based on Au/MoS_2/Au nanolayer on the polyethylene terephthalate (PET) to detect HIV-1 (Shin, Yoon, Yi, Lee, & Choi, 2019). MoS_2 NPs (2 nm) were synthesized by Wang *et. al.,* and explored its electro-catalytical behavior towards the reduction of hydrogen peroxide (H_2O_2), and developed an extremely sensitive biosensor for H_2O_2 detection (Wang et al., 2013). Due to its novel electroactive properties, Geng *et al.* fabricated a non-enzymatic glucose sensor based on Ni-doped MoS_2 NPs fixed to RGO (Geng, Bo, & Guo, 2017). Nevertheless, the electrochemical detection and catalytic activity of such nanomaterials are still limited and need to be further explored. These factors motivated us to investigate the efficiency of $nMoS_2$ NPs in the fabrication of electrochemical immunosensors.

As a proof-of-concept, in the present study, an electrochemical approach based on antibodies has been developed for the first time to detect beta-lactam antibiotic, AMP. Indium tin oxide (ITO) electrodes altered with $nMoS_2$ NPs have been used as the substrate to immobilize the anti-AMP antibodies towards highly sensitive detection of AMP from spiked food samples. The change in the MoS_2 interface current was caused by the specific binding of AMP to the antibodies immobilized onto the $nMoS_2$ NPs/ITO electrode. Other antibiotics such as norfloxacin, ofloxacin, and ciprofloxacin were used in this experiment to test the specificity of the immunosensors. This immunosensor exhibits high sensitivity [41.81 μA (log μg $mL^{-1})^{-1}$], wide linear range (0.0325–64 μg mL^{-1}), the outstanding detection limit (0.028 μgmL^{-1}), and good specificity with excellent recovery and no significant signals to non-target antibiotics and other interferents. Thus, the proposed immunosensor showed a promising sensing platform towards AMP detection with low cost that might prove beneficial for the on-site detection of chemical or biological molecules. These synthesized $nMoS_2$ NPs have significant physio-electrochemical properties, resulting in a highly effective electrochemical immunosensor for the AMP detection having excellent sensitivity, stability, repeatability, and selectivity.

2. Experimental section

2.1. Materials and chemicals

Ascorbic acid (Vit-C), cholesterol, bovine serum albumin, glucose, 1-(3-(dimethylamino)-propyl)-3-ethylcarbodiimide hydrochloride (EDC), (3-aminopropyl) trimethoxysilane [APTES], acetonitrile was obtained from Sigma Aldrich, India. Ethanol, H_2O_2, and acetone were purchased from Fisher Scientific. High purity sodium molybdatedihydrate [$Na_2MoO_4{\cdot}2H_2O$], thiourea [CH_4N_2S], ampicillin (AMP), sodium phosphate monobasic anhydrous ($NaHPO_4$), potassium ferricyanide, potassium ferrocyanide, sodium hydroxide pellets (NaOH), sodium phosphate dibasic dihydrate (NaH_2PO_4), norfloxacin, ofloxacin, and ciprofloxacin were procured from SRL Limited. *N*-hydroxysulfosuccinimide (NHS) were got from HiMedia. The ITO glass substrate was bought from Blazers, UK. All the chemicals were of analytical grade and further used without purification. The phosphate buffer solution (PBS; 0.2 M) of pH 7.0 was made fresh with $NaHPO_4$ and NaH_2PO_4 in millipore water (milli-Q) and stored at 4℃ for further use. The ampicillin specific antibodies (anti-AMP Abs) were taken from Ram Abuknesha, King's College, London, UK of Sigma, and diluted in PBS (pH 7.0). Further, the whole study was done in Milli-Q.

2.2. Instrumentation

The crystalline nature and phase structural information were studied using XRD [RigakuMiniflex 600 (Japan) diffractometer] with a monochromatic X-ray beam (λ = 1.5406 Å) having Cu-Kα radiation. The spectra recorded in an angular range from 5 to 70° (2θ), having a step size of 5° (2θ) at room temperature, and the acquired data were assessed through EVA software. The Raman spectroscopy of $nMoS_2$NPs in the range of 500–2000 cm^{-1} was carried out on EnSpectr R532, USA laser of WITEC system. The functional groups present in $nMoS_2$ NPs modified with APTES, anti-AMP, and BSA on ITO electrodes were studied *via* Fourier transform infrared spectroscopy (FT-IR, Perkin Elmer, US). Structural and morphological analysis was done using transmission electron microscopy (TEM, JEM-2200 FS, Jeol, Japan) and field emission-scanning electron microscopy (FE-SEM). Firstly, sample preparation for HR-TEM was done by dispersing MoS_2 in ethanol by ultrasonication and then spread on a copper grid and dried at room temperature. To get the topographical data of ITO, APTES/$nMoS_2$/ITO, anti-AMP/APTES/$nMoS_2$/ITO, and BSA/anti-AMP/APTES/$nMoS_2$/ITO immunoelectrode; the study of atomic force microscopy (AFM) was carried out. Further, the drop shape analyzer [KRUSS, Germany] was used for the water contact angle study to observe the hydrophilic/ hydrophobic nature of ITO, APTES/$nMoS_2$/ITO, anti-AMP/APTES/$nMoS_2$/ITO, and BSA/anti-AMP/APTES/$nMoS_2$/ITO electrodes. All the electrochemistry characterization [differential pulse voltammetry

(DPV), EIS, and cyclic voltammetry (CV)] of fabricated electrodes were conducted using an Autolab, Galvanostat/Potentiostat electrochemical analyzer (EcoChemie, The Netherlands) and analyzed by the NOVA (version 1.10) software. All the electrochemical experiments were performed trice (n = 3) using PBS solution (0.2 M) having redox species acting as redox coupler with 0.9% NaCl. The utilization of a three-electrode system was done where silver-silver chloride (Ag/AgCl), platinum (Pt), and modified ITO coated glass substrate acted as a reference, counter, and working electrode, respectively.

2.3. Synthesis and functionalization of $nMoS_2$ NPs

The $nMoS_2$NPs were made at low temperature by utilizing a one-step hydrothermal process. For this, 1 g of sodium molybdate dihydrate [$Na_2MoO_4{\cdot}2H_2O$] and 1.9 g of thiourea [CH_4N_2S] were dissolved in 40 mL of Mili-Q water for 20 min under vigorous stirring to form a homogenous solution. After this, the solution was ultra-sonicated for 30 min and transferred to a 100 mL Teflon that was hydrothermally retained for 24 h at 200°C. The black precipitate was collected by centrifugation, followed by washing with Mili-Q water/absolute ethanol, and finally dried in an oven for 12 h at 80°C to obtain $nMoS_2$ NPs. Then, with the help of the mortar-pestle, crushing of the product was carried out to get the fine powder for further characterization and use.

APTES was used for the functionalization of $nMoS_2$. A solution of $nMoS_2$ in 10 mL of isopropanol was dispersed with continuous stirring at 60℃. 200 μL of APTES (98%) was added to this dispersion and continuously stirred at 300 rpm for 48 h. Finally, the product was washed with the Mili-Q water for removing the excess APTES, dried (60℃), and kept in a dry place to get APTES functionalized $nMoS_2$ (APTES/$nMoS_2$).

2.4. Electrophoretic deposition of APTES/$nMoS_2$ NPs on ITO electrode (APTES/$nMoS_2$/ITO)

ITO coated glass substrates of almost the same size, i.e.,1.5 × 0.5 cm, were taken, and hydrolyzation was performed in the solution mixture of H_2O: NH_4OH: H_2O_2 having a ratio of 5:1:1 at 80 ℃ for 1 h followed by washing with Mili-Q water/ethanol and dried in an oven at 60 ℃. Before deposition, a stock solution (5 mg mL^{-1}) was prepared containing 10 mg of APTES/$nMoS_2$ in 2 mL of acetonitrile *via* ultra-sonication. Here, platinum wire and ITO were used as a reference and working electrode, respectively, placed 1 cm apart in the glass cell. The surface area of the APTES/$nMoS_2$/ITO electrodes was also optimized and estimated to be 0.25 cm^2. Next, a solution containing an optimized mixture of 3 mL acetonitrile, 100 μL stock solution of APTES/$nMoS_2$, and 20 μL of Mg $(NO_3)_2$ was taken in a glass cell, followed by ultra-sonication for 30 s. The APTES/$nMoS_2$ was deposited *via* an electrophoretic deposition (EPD) technique onto the pre-hydrolyzed ITO using a Genetix, GX300C instrument where a DC potential of 60 V was applied for obtaining a thin, uniform film of APTES/$nMoS_2$ on ITO electrode (APTES/$nMoS_2$/ITO) for 1 min after optimization. The fabricated electrode was then washed with Mili-Q water, followed by drying at 25 °C overnight.

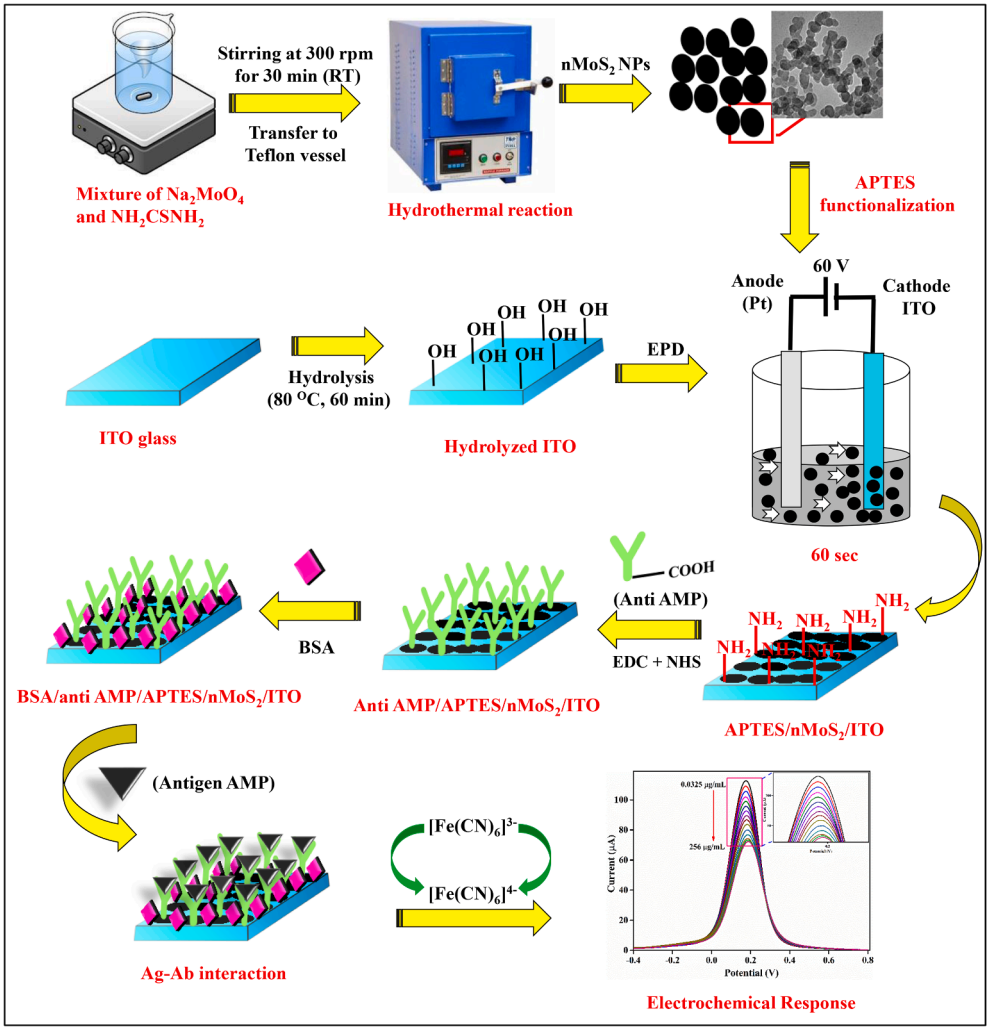

Scheme 1. Schematic representation of the synthesis of $nMoS_2$ NPs and development of BSA/anti-AMP/APTES/$nMoS_2$/ITO immunoelectrode for AMP detection.

2.5. Fabrication of immuno-sensing platform (anti-AMP/APTES/nMoS$_2$/ITO)

The APTES/nMoS$_2$/ITO electrode acted as the immunosensing interface for the development of the biosensor. For this, preparation of anti-AMP (1:10 of 10 mg mL^{-1}), NHS (0.1 M) and EDC (0.4 M) solutions were prepared in PBS of pH 7.0. The final solution of anti-AMP: EDC (activator): NHS (coupling agent) was made by mixing them in a ratio of 2:1:1 followed by incubation for 45 min before use. Subsequently, 30 μL of this was drop casted on APTES/nMoS$_2$/ITO by maintaining it at 25 °C in a humid chamber for nearly 6 h followed by washing with PBS (200 μL) of pH 7.0 to get rid of the free antibodies. The anti-AMP molecules were bound to APTES/nMoS$_2$/ITO electrode covalently by forming a bond between the carboxyl group (–COOH) on the Fc portion of the anti-AMP and –NH$_2$ group of APTES molecules. The activation of –COOH of anti-AMP by EDC during the reaction generated an unstable O-acylisourea ester that reacted with NHS to form an amine-reactive NHS ester (stable intermediate product). This activation of anti-AMP by NHS aids in connecting –NH$_2$ groups of APTES molecules for generating an amide bond. Further, the non-specific places were blocked using 10 μL of 2% BSA of anti-AMP/APTES/nMoS$_2$/ITO immunoelectrode and stored for 2 h in the humid chamber. Later, washing of developed BSA/anti-AMP/APTES/nMoS$_2$/ITO immunoelectrode was carried out with PBS (100 μL) and kept for further use at 4℃. Scheme 1 depicts the step-wise development of the BSA/anti-AMP/APTES/nMoS$_2$/ITO electrode.

2.6. Preparation of AMP dilutions

Various AMP concentrations were prepared in the range from 0.0325 μg mL^{-1} to 256 μg mL^{-1} in 0.2 M PBS of pH 7.0. All the experiments of immunosensor were performed *via* the technique of DPV in PBS containing $[Fe(CN)_6]^{3-/4-}$. The developed immunosensor was used for the testing of real sample analysis *via* spiked food samples.

2.7. Preparation of real samples

Three food samples, such as milk, orange juice, and tap water, were taken for spiked real sample analysis. Milk and orange juice were bought from a local market of the JNU campus. The 100 mL of pure milk requires pre-treatment with 6 mL of 5 M methanol and 1 mL of 20 mM trichloroacetic acid mixed well and centrifuged at 10,000 rpm for 15 min at 25 °C. The supernatant was then filtrated slowly to get the test sample. The filtration of orange juice and tap water (taken from own laboratory) followed by centrifugation at 10,000 rpm for 20 min was also carried out. The samples were first tested for the presence of AMP. When there was no change in the signal observed, they were spiked. The spiked samples of milk, orange juice, and tap water were prepared by mixing 20 μL of treated milk, orange juice, and tap water in 3 mL of PBS containing redox coupler with different AMP concentrations (0.0625, 0.5, 2, 8, 16 and 64 μg mL^{-1}). The spiked samples were being utilized for the sensing on BSA/anti-AMP/APTES/nMoS$_2$/ITO immunosensor.

3. Results and discussions

3.1. Chemistry behind nMoS$_2$ synthesis

In the present study, a simple hydrothermal method was used for synthesizing of nMoS$_2$NPs. These methods have several advantages compared to other traditional and non-traditional methods due to economical, facile, and less consumption of chemicals (Pourabbas & Jamshidi, 2008). In the process of hydrothermal synthesis, the material gets precipitated directly from the solution, thereby maintaining the rate, nucleation, aging, morphology, size, and control over growth of the nanoparticles, which is not in the case of several other methods (G. Wang, Wang, Zhang, Fei, & Zhang, 2004). It is described in many reports that this process doesn't require large scale production with quality crystals, seed, catalyst, toxic template, or surfactant and could be merged with other methods (Yadav, Dhiman, Lakshmi, Berlina, & Solanki, 2020).

During the hydrothermal reaction, there is perhaps hydrolysis of thiourea taking place forming NH_3, H_2S, HNCS, and CS_2 at high pressure and low-temperature conditions accountable for reducing Mo(VI) to Mo (IV) and synthesis of nMoS$_2$NPs take place. According to the experimental conditions and literature survey (Feng et al., 2009), the following reaction is a complex process containing three steps:

(i) NH_2CSNH_2 hydrolysis for forming H_2S;
(ii) Mo (VI) reduction to form Mo (IV);
(iii) nMoS$_2$NPs formation.

The MoS$_2$ nucleation, followed by its subsequent aggregation on the surface of the substrate, occurred directly during the hydrothermal reaction. Also, enhancement in reaction time converted MoS$_2$ nucleation into a nanoparticle-like structure. The reaction process for the synthesis of nMoS$_2$NPs are described in the following equations:

$$CS(NH_2)_2 + 2H_2O \rightarrow 2NH_3 + CO_2 + H_2S. \quad (1)$$

$$4Na_2MoO_4 + 15CS(NH_2)_2 + 6H_2O \rightarrow 4MoS_2 + Na_2SO_4 + 6NaSCN + 24\,NH_3 + 9\,CO_2 \quad (2)$$

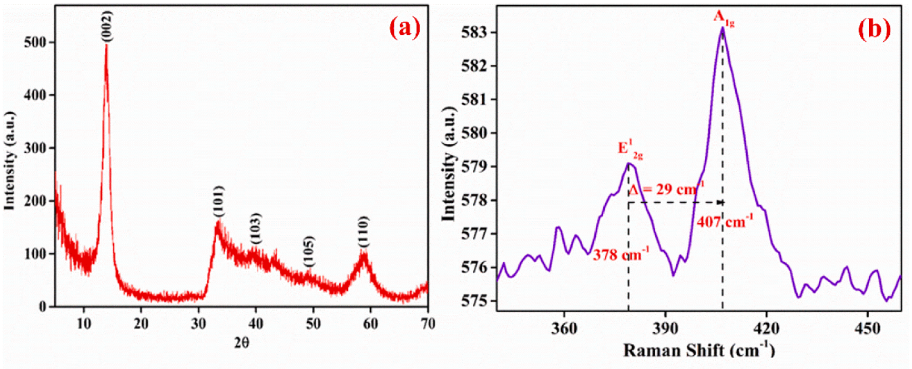

Fig. 1A. (a) XRD pattern of nMoS$_2$NPs, (b) Raman spectrum of nMoS$_2$NPs.

3.2. Structural and morphological characterizations

3.2.1. XRD analysis

The XRD was conducted to investigate the structure, crystallinity, and phase of $nMoS_2$ NPs. Fig. 1A (a) depicts the XRD plot of the hydrothermally synthesized $nMoS_2$NPs having a 2θ angle in a range of 5 to 70°. The various characteristic peaks at 14°, 33.5°, 39.9°, 49.4° and 58.9°corresponding to the planes (0 0 2), (1 0 1),(1 0 3), (1 0 5) and (1 1 0) respectively, were obtained for the hexagonal structure of $nMoS_2$NPs, i.e., the most stable form of $nMoS_2$ at room temperature (JCPDS data card no. 37–1492) (Singhal, Khanuja, Chaudhary, Pundir, & Narang, 2018). By applying the Debye-Scherer formula denoted in Eq. (3), the crystallite size of $nMoS_2$NPs was calculated to be about 6 nm, corresponding to the strongest peak (0 0 2).

$$D = \frac{k\lambda}{\beta\cos\theta} \quad (3)$$

Where, λ = 1.540 Å (Cu-K_α wavelength of source), θ = diffraction angle, β = full width at half maximum (FWHM) of the diffraction peak (s), D = crystallite size, and k = crystallization constant (~0.94).

3.2.2. Raman analysis

The Raman spectrum of synthesized $nMoS_2$ NPs is shown in Fig. 1A (b). The characteristic peaks were obtained at 382 cm^{-1} (E^1_{2g}) and 407 cm^{-1}(A_{1g}), corresponding to the in-plane and out of plane phonon modes of $nMoS_2$. The characteristic difference between these peaks is around 25 cm^{-1}, suggesting that stacking of NPs occurred together *via* 5 or more layers of $nMoS_2$. These two prominent peaks show that synthesized $nMoS_2$NPs have a 2H-MoS_2 structure (Lee et al., 2010).

3.2.3. Transmission electron microscopy (TEM) analysis

Further, the size and morphology of $nMoS_2$NPs were studied using TEM [Fig. 1B (a-c)]. Fig. 1B (a-b) shows the typical TEM image of the hydrothermally prepared $nMoS_2$NPs having irregular and nearly spherical shaped particles that look like potatoes. To precisely quantify the particle size distribution, the histogram is configured with a Gaussian function. [Fig. 1B(c)]. The average size of the NPs was measured to be 25–30 nm.

3.2.4. Field emission-scanning electron microscopy (FE-SEM) analysis

The synthesized APTES/$nMoS_2$NPs were deposited onto ITO electrodes electrophoretically, followed by immobilization of anti-AMP and BSA. To visualize the change in surface morphology after biomolecule immobilization (anti-AMP and BSA), the fabricated APTES/$nMoS_2$/ITO, anti-AMP/APTES/$nMoS_2$/ITO, and BSA/anti-AMP/APTES/$nMoS_2$/ITO electrodes were examined by FE-SEM at different magnifications (1 μm, 500 nm, and 200 nm) as shown in Fig. S2. As seen in the FE-SEM image, Fig. S2 (a, b, c) confirms that the APTES/$nMoS_2$NPs surface had a porous matrix, which provided a high surface/volume ratio that provided greater immobilization area for anti-AMP and facilitated amplification of electrochemical signals. This may be attributed to the uniform deposition of APTES/$nMoS_2$ on the ITO substrate, where APTES/$nMoS_2$ developed through the proposed method consists of nanoparticles that are tightly stacked together. The surface morphology of the APTES/$nMoS_2$/ITO electrode was changed upon the attachment of anti-AMP due to the presence of globules on the surface of anti-AMP/APTES/$nMoS_2$/ITO immunoelectrode [Fig. S2 (d, e, f]. The occurrence of this globule shaped structure was due to the macromolecule size of anti-AMP, confirming the anti-AMP attachment to APTES/$nMoS_2$/ITO electrode. Also, in comparison to Fig. S2 (a, b, c), the surface roughness of

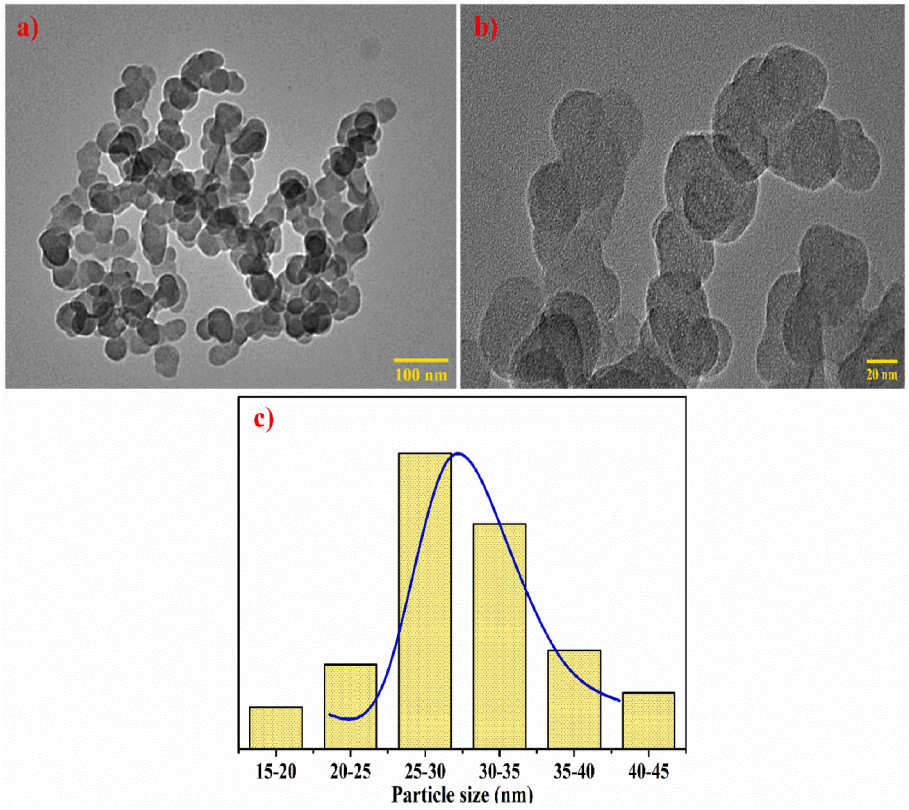

Fig. 1B. (a, b) TEM images at different magnifications, (c) particle size distribution.

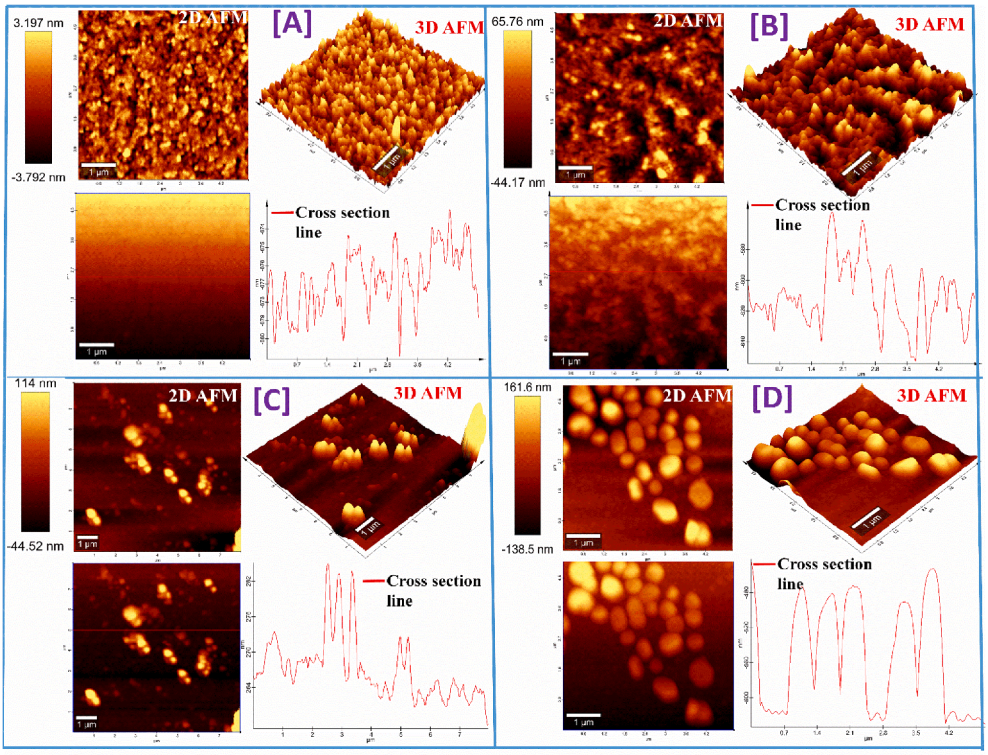

Fig. 2. AFM images of bare ITO electrode (A), APTES/nMoS$_2$ modified ITO electrode (B), anti-AMP antibodies immobilized electrode surface (C), and after BSA immobilization (D).

the anti-AMP/APTES/nMoS$_2$/ITO electrode seems to be smoother. This smoothness indicates the presence of anti-AMP biomolecules on the fabricated immunoelectrode surface. However, further functionalization of anti-AMP/APTES/nMoS$_2$/ITO immunoelectrode with BSA modified the morphology from globules to a more homogeneous smooth structure, showing that all the unbound sites of electrode surface area covered by BSA completely [Fig. S2 (g, h, i].

3.2.5. *Atomic force microscopy (AFM)*

The AFM images with the height profiles were obtained in the tapping mode to study the surface morphology, uniformity, thickness, and roughness of bare ITO modified with electrophoretically deposited APTES/nMoS$_2$/ITO, anti-AMP/APTES/nMoS$_2$/ITO, and BSA/anti-AMP/APTES/ nMoS$_2$/ITO electrodes as shown in Fig. 2(A-D). The AFM image of bare ITO with an average roughness value of −694.49 nm was shown in Fig. 2 (A). Fig. 2 (B) depicts the AFM image of the APTES/nMoS$_2$/ITO film having a smooth surface and granular topography with dense composite smoothly spread on the ITO surface. The average roughness value was found as 0.699 nm. This is because of the uniform electrophoretic deposition of functionalized nMos$_2$NPs on the ITO surface due to intermolecular forces of attraction between ITO and APTES/nMoS$_2$ electrode. Further, a change in the topography of the electrode (globular) occurred after the covalent attachment of anti-AMP with enhancement in average roughness value of 0.940 nm, as shown in Fig. 2 (C). The increment in roughness may be ascribed to the globular Y-shaped structure of the antibodies, revealing successful attachment of biomolecules to APTES/nMoS$_2$/ITO electrode. As observed in Fig. 2 (D), there is a further decrease in the porous property of the surface of the electrode. An uniform surface was seen, which depicts the attachment of BSA molecules to anti-AMP/APTES/nMoS$_2$/ITO electrode surface. The average surface roughness value at this step was found to be −608 nm, which supported the smooth surface formation. The non-specific adsorption of BSA to bare sites of anti-AMP/APTES/nMoS$_2$ may be ascribed to the cause of decreased roughness hence forming a highly uniform immunoelectrode surface.

3.2.6. *Fourier transform infrared spectroscopic (FT-IR) analysis*

FT-IR analysis was conducted to verify MoS$_2$ synthesis and immobilization of anti-AMP and BSA on APTES/nMoS$_2$ /ITO electrode by examining the presence of various functional groups and formation of bonds. Fig. S3 shows the FT-IR spectra of (a) nMoS$_2$/ITO, (b) APTES/nMoS$_2$/ITO, (c) anti-AMP/APTES/nMoS$_2$/ITO and (d) BSA/anti-AMP/APTES/nMoS$_2$/ITO immunoelectrode. In Fig. S3 (a), the broad absorption bands at 552 cm^{-1}, 857 cm^{-1}, 1416 cm^{-1} are shown that corresponds to nMoS$_2$NPs (Pua, Chia, Zakari, Liew, Yarmo, & Huang, 2010). The band from 1591 to 1303 cm^{-1} are depicted in Fig. S3 (b), which corresponds to N—H bending for 1° amine (Srivastava et al., 2013) while in the case of anti-AMP/APTES/nMoS$_2$/ITO [Fig. S3 (c)], the peak at 1428 cm^{-1} is ascribed to stretching vibration of C—N bond occurring between Fc regions of anti-AMP and –NH$_2$ group of APTES/nMoS$_2$ NPs (Cai & Singh, 2004). The sharp peak at 1642 cm^{-1} also appeared due to —C═O bending vibration of amide bond (O═C—N—H). The peak at 870 cm^{-1} got disappeared, which attributes to the —NH$_2$ group of APTES/nMoS$_2$/ITO after BSA immobilization as shown in the case of BSA/anti-AMP/APTES/nMoS$_2$/ITO [Fig. S3 (d)], confirming the blocking of unbounded sites onto anti-AMP/APTES/nMoS$_2$/ITO electrode (Tiwari, Gupta, Bagbi, Sarkar, & Solanki, 2017) Though, less intensity, and widening of peaks occur for BSA/anti-AMP/APTES/nMoS$_2$/ITO electrode that further approves the blockage of unbounded sites on immunoelectrode by BSA. Thus, the spectra confirmed the successful formation of thin films of nMoS$_2$ NPs on the surface of ITO and its functionalization with APTES and immobilization and blocking with anti-AMP, and BSA, respectively.

3.2.7. *Contact angle (CA) analysis*

The CA studies based on the sessile drop method were conducted to determine the hydrophobic/hydrophilic surface behaviour of the fabricated electrodes after modification at each step (Fig. S4). The CA (75.5)

for the bare hydrolyzed ITO electrode [Fig. S4 (a)] indicated hydrophilic nature. After EPD of APTES/nMoS$_2$ onto the ITO electrode, the CA increased to 99.2° [Fig. S4 (b)] indicating the slightly hydrophobic nature of the APTES/nMoS$_2$/ITO electrode providing the favourable environment for immobilization of anti-AMP antibodies. Further, CA was found to decrease, i.e., 13.1° [Fig. S4 (c)] after immobilization of anti-AMP on APTES/nMoS$_2$/ITO electrode, which depicts the increase in hydrophilic behaviour (Pavia, Lampman, Kriz, & Vyvyan, 2014). This hydrophilic nature helps in the enhancement of AMP/antigen attachment in an aqueous PBS buffer and improves sensitivity (Yadav et al., 2020).

4. Electrochemical studies

4.1. Optimization of electrochemical studies

Numerous factors affect the electrochemical performance of the AMP immunosensor. At first, the impact of $[Fe(CN)_6]^{3-/4-}$ on the CV of both APTES/nMoS$_2$/ITO and BSA/anti-AMP/APTES/nMoS$_2$/ITO immunoelectrodes shows in Fig. S5. It can be observed from Fig. S5(a) and (b)) that the CV in PBS does not show strong oxidation and reduction peaks. The addition of $[Fe(CN)_6]^{3-/4-}$ helped in accelerating the charge carrier movement by displaying strong redox peaks in both APTES/nMoS$_2$/ITO and BSA/anti-AMP/APTES/nMoS$_2$/ITO electrodes (Kumar, Sharma, Maji, & Malhotra, 2016). Therefore, PBS containing $[Fe(CN)_6]^{3-/4-}$ mediator has been chosen as the working redox buffer for further studies.

The DPV method has been utilized to examine the electrochemical response occurring between BSA/anti-AMP/APTES/nMoS$_2$/ITO immunoelectrode and pH (6.0 to 8.0) in PBS(0.2 M) having $[Fe(CN)_6]^{3-/4-}$ at the scan rate of 50 mVs^{-1} [Fig. S6 (a)]. The results showed a rise in DPV peak current upon increasing the pH range from 6.0 to 7.0, whereas the peak current decreases on further increasing the pH from 7.5 to 8.0. Hence, the highest DPV peak current intensity occurred with PBS at neutral pH 7.0. This might be possible because natural forms of biological molecules like enzymes, antibodies, antigens, amino acids, etc., exist at neutral pH with high specific activity. Also, denaturation of immobilized proteins and antibodies occurs in a highly basic or acidic atmosphere due to the OH^- or H^+ ions interaction on the amino acid sequence of the antibodies (Kumar, et al., 2016). This is a trivial idea that biomolecules could also have shown a high current response at pI (isoelectric point), whereas low pI negatively impacts the electrochemical behavior. Thus, PBS of pH 7.0 was the most suitable and optimal pH for Ag-Ab immuno-complex formation and, therefore, was selected for further electrochemical studies.

The DPV peak current of the BSA/anti-AMP/APTES/nMoS$_2$/ITO immunoelectrode was measured at an optimal AMP concentration to evaluate the effect of Ag-Ab interaction on the incubation time. Fig. S6 (b) depicts the different current values achieved on AMP interaction with the BSA/anti-AMP/APTES/nMoS$_2$/ITO immunoelectrode through DPV for various incubation times from 0 to 30 min. We observed a fast decrease in peak current with an increase in incubation time, i.e., from 0 to 25 min, and become saturated after 25 min due to anti-AMP-AMP immune-complex formation, showing maximum AMP attachment to the surface of the electrode. Thus, 25 min was selected as the optimal Ab-Ag incubation time for further studies.

Besides this study, DPV was used to determine the optimal concentration of the anti-AMP bound to the APTES/nMoS$_2$/ITO electrode. The electrode peaks current increased with an increasing anti-AMP concentration (1–35 µL of 1:10 dilution) and became saturated at 30 µL concentration, after which no increment of current intensity was observed as shown in Fig. S6 (c). Therefore, 30 µL of 1:10 Ab dilution was chosen for further immunosensor studies.

Fig. S6 (d) displays the changes in DPV peak current of the BSA/anti-AMP/APTES/nMoS$_2$/ITO electrode with BSA concentration (2%) at diverse volumes from 1 to 12 µL. The decrease in peak current was observed from 1 to 10 µL, after which it gets saturated, showing 10 µL (2%) was selected as the optimum BSA (2%) concentration for further

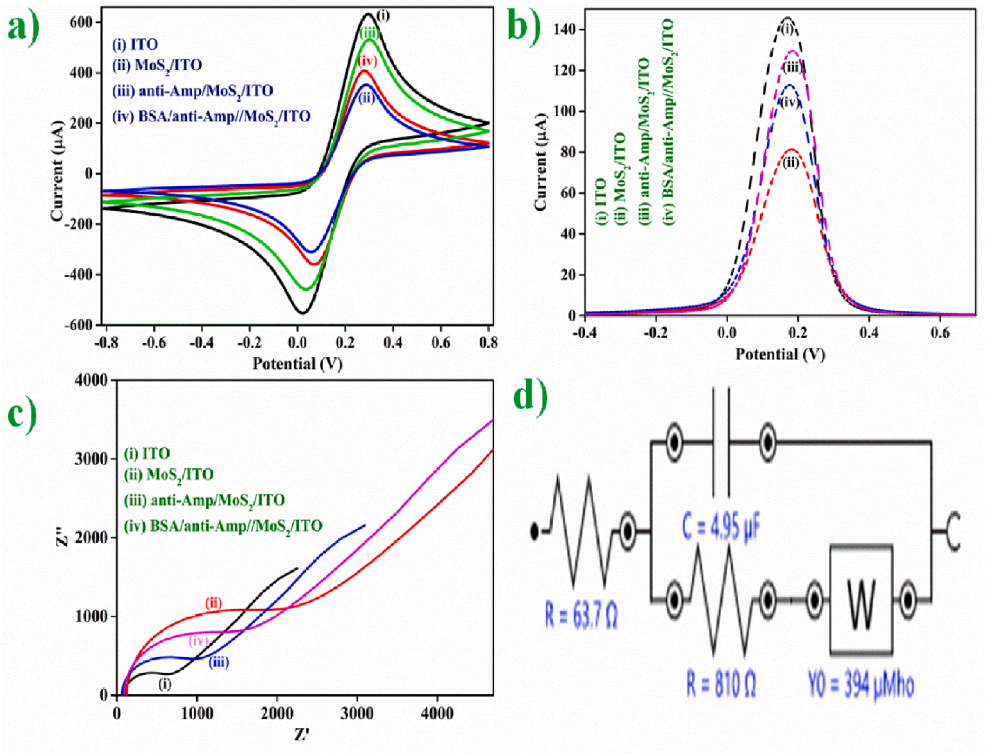

Fig. 3. (a) CV; (b) DPV; and (c) EIS of (i) ITO, (ii) APTES/nMoS$_2$/ITO, (iii) anti-AMP/APTES/nMoS$_2$/ITO, and (iv) BSA/anti-AMP/APTES/nMoS$_2$/ITO electrodes; (d) Nyquist circuit diagram from EIS.

experiments.

Hence, the optimized experimental parameter for these assays was as follows: 30 μL of incubating concentration of 1:10 dilution of anti-AMP, PBS (0.2 M,) of pH 7.0 containing redox probe $[Fe(CN)_6]^{3-/4-}$, incubation time of 30 min for AMP detection, and 10 μL of incubating concentration of 2% BSA.

4.2. Electrochemical studies of the fabricated immunosensor

The techniques that were used to study the electron transfer properties of various $nMoS_2$NPs-based modified electrodes were electrochemical impedance spectroscopy (EIS), DPV, and CV in PBS solutions of pH 7.0, having $[Fe(CN)_6]^{3-/4-}$. Fig. 3 (b) shows the DPV responses of ITO, APTES/$nMoS_2$/ITO, anti-AMP/APTES/$nMoS_2$/ITO, and BSA/anti-AMP/APTES/$nMoS_2$/ITO immunoelectrodes, respectively in the potential range of −0.4 to 0.8 V at a scan rate of 50 mVs^{-1} using a step potential of 5 mV with at interval of 0.5 ms. The maximum current value in the case of ITO was 145.69 μA (curve i), which decreased in APTES/$nMoS_2$/ITO electrode to 81.33 μA (curve ii) after electrophoretic deposition of $nMoS_2$ nanoparticles on ITO, showing a slow transfer of electrons between APTES/$nMoS_2$/ITO and electrolyte interface. After anti-AMP attachment on APTES/$nMoS_2$/ITO immunoelectrode, an increase in peak current was observed, i.e., 129.60 μA (curve iii), signifying the fast transfer of electrons to the surface of the electrode. This increase in peak current occurred when the surface of the APTES/$nMoS_2$/ITO electrode gets functionalized with the anti-AMP. The APTES/$nMoS_2$ may be acting as a mediator at the electrode surface of ITO, causing a remarkable decrease in electron tunneling distance between the electrode and the antibodies. Also, rapid diffusion of electrons towards the immunoelectrode was due to the non-covalent bonding between the $[Fe(CN)_6]^{3-/4-}$ and free position of $–NH_2$ terminal of anti-AMP (Yadav et al., 2020). BSA acted as a blocking agent for blocking the non-specific active sites of the APTES/$nMoS_2$ surface. After the BSA attachment, there is a decrease in the peak current, i.e., 112.76 μA (curve iv), due to the insulating behavior of BSA molecules and non-specific attachment of BSA on the exposed surface of APTES/$nMoS_2$ of the anti-AMP/APTES/$nMoS_2$/ITO electrodes. Further, the CV of ITO, APTES/$nMoS_2$/ITO, anti-AMP/APTES/$nMoS_2$/ITO, and BSA/anti-AMP/APTES/$nMoS_2$/ITO immunoelectrodes were performed in the potential range of −0.8 to + 0.8 V at a scan rate of 50 mV s^{-1} showing similar results as that of DPV in Fig. 3 (a). These results combined with the contact angle, AFM, and FE-SEM studies, revealing stepwise, successful fabrication of immunoelectrode.

4.2.1. EIS studies

The electrochemical impedance spectroscopic studies of ITO, APTES/MoS_2/ITO, anti-AMP/APTES/MoS_2/ITO, and BSA/anti-AMP/APTES/MoS_2/ITO have been done in PBS solution containing $[Fe(CN)_6]^{3-/4-}$ in the frequency range of 100 kHz to 10 Hz [Fig. 3 (c)]. The semicircle of the Nyquist plot shows the charge transfer resistance (R_{ct}) of various electrodes, which depends on the dielectric features of the electrolyte and surface of the electrode. Fig. 3 (c) and 3 (d) shows the Nyquist plot of ITO glass substrate (i), APTES/MoS_2/ITO (ii), anti-AMP/APTES/MoS_2/ITO (iii) and BSA/anti-AMP/APTES/MoS_2/ITO (iv); and Nyquist circuit diagram, respectively.

The value of R_{ct} was obtained as 482 Ω for the ITO glass substrate (curve i), which is the lowest. However, there is a significant increase in the value of R_{ct} 1720 Ω after the deposition of APTES functionalized $nMoS_2$ NPs onto ITO surface (curve ii), indicates the low electrical conductivity of APTES functionalized $nMoS_2$ NPs and slow diffusion of $[Fe(CN)_6]^{3-/4-}$ to the surface of the electrode. However, after the covalent immobilization of anti-AMP to the free NH_2 sites of APTES functionalized $nMoS_2$ NPs, the value of R_{ct} drastically decreases to 810 Ω for anti-AMP/APTES/MoS_2/ITO (curve iii). This decrease in the value of R_{ct} can be assigned to the spatial orientation of anti-AMP molecule onto electrode surface that facilitate increased charge transfer process between $[Fe(CN)_6]^{3-/4-}$ and free available functional group (-NH_2) of anti-AMP (Kumar, Sharma, et al., 2016). The value of R_{ct} increases (1250 Ω; curve iv) after immobilizing BSA on the anti-AMP/APTES/MoS_2/ITO immunoelectrode owing to the insulating nature and macromolecular structure of BSA that hamper the transfer of charge between the surface of the electrode and $[Fe(CN)_6]^{3-/4-}$.

The K_{ct} for all respective electrodes was calculated using Eq.(4):

$$\mathrm{Kct} = \frac{RT}{n^2F^2\mathrm{ARct[S]}} \tag{4}$$

Where [S] is the concentration of redox probe (mol cm^{-3}), F is Faraday constant; A is the surface area of the electrode (cm^2), n is the no. of electrons transferred/molecule of the $[Fe(CN)_6]^{3-/4-}$, T is the absolute temperature, and R is gas constant. The K_{ct} value of the ITO electrode was found as 4.42×10^{-7}, while in the case of APTES/$nMoS_2$/ITO, the value of K_{ct} decreases to 1.24×10^{-7}, exhibiting the slower electron transfer between the APTES/MoS_2/ITO electrode and $[Fe(CN)_6]^{3-/4-}$. After attachment of anti-AMP antibodies, the K_{ct} value increases to 2.62×10^{-7} shows the fast electron exchange between immunoelectrode and redox species. However, after the BSA immobilization on anti-AMP/APTES/$nMoS_2$/ITO immunoelectrode, the value of K_{ct} decreases to 1.70×10^{-7} due to its insulating nature, which resists the transfer of electrons.

The Time constant (τ) for each electrode has been calculated using equation (5):

$$R_{ct} \cdot C_{dl} = 1/2\pi\ f_{max} = \tau \tag{5}$$

After the EPD of APTES/$nMoS_2$ on the ITO substrate (2.356×10^{-3} s), an abrupt increase in the time constant value was found compared to the ITO glass substrate 5.744×10^{-3} s. It reveals the sluggish diffusion of ferro-ferri ions at the electrolyte and APTES/$nMoS_2$/ITO electrode interface. The immobilization of anti-AMP on to the APTES/$nMoS_2$/ITO electrode result in a decrease of τ value 4.009×10^{-3} s due to the rapid diffusion of Ferro-ferri ions. After the BSA immobilization, the value of τ again increases 4.637×10^{-3} s due to the insulating behavior of BSA. ElS characteristics, including heterogeneous electron transfer rate constant (K_{ct}) and time constant (τ), of different electrodes, were given in Table S1.

4.3. Scan rate studies

The CV responses in PBS having redox species was used to study the interfacial kinetics of APTES/$nMoS_2$/ITO electrode and BSA/anti-AMP/APTES/$nMoS_2$/ITO immunoelectrode versus scan rate (10–100 mVs^{-1}) at the interface of the electrode surface and electrolyte [Figs. S7 and S8]. We observed similar behavior that the magnitudes of both cathodic (Ipc) and anodic (Ipa) peak currents exhibit a linear relationship with increasing scan rate values, indicating the given electrochemical reaction is a diffusion-controlled process between electrode and electrolyte (Tiwari et al., 2017). Figs. S7 and S8 inset (upper) shows the magnitude of anodic (Ipa) and cathodic (Ipc) peak currents vs. square root of scan rate in which current of both electrodes linearly increased with increase in scan rates.

The intercepts and slopes have been calculated from linear curve fitting, which gives the following equations-

$$\mathrm{Ipc}_{(\mathrm{APTES/nMoS2/ITO})} = -\left[30.86\,\mu\mathrm{A(s/mV)} \times (\mathrm{scan\ rate[mV/s]})^{1/2}\right] - 67.29\,\mu\mathrm{A},\ R^2 = 0.988 \tag{6}$$

$$\mathrm{Ipa}_{(\mathrm{APTES/nMoS2/ITO})} = \left[39.69\,\mu\mathrm{A(s/mV)} \times (\mathrm{scan\ rate[mV/s]})^{1/2}\right] - 48.11\,\mu\mathrm{A},\ R^2 = 0.992 \tag{7}$$

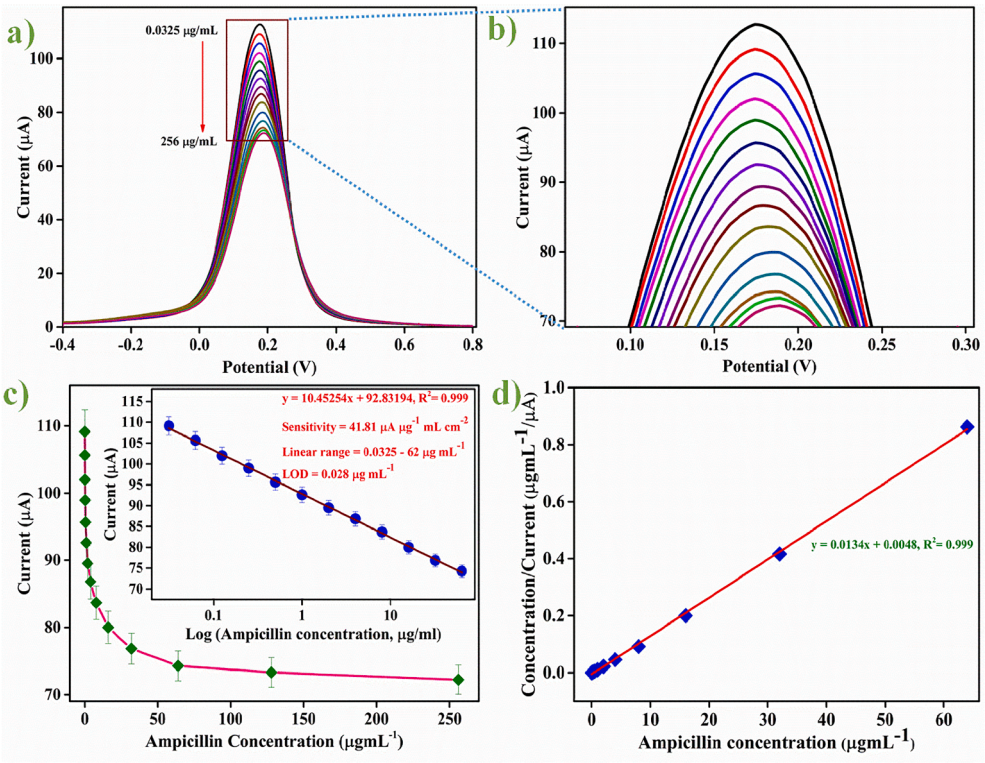

Fig. 4. (a) Electrochemical response analysis of BSA/anti-AMP/APTES/nMoS$_2$/ITO immunosensor versus concentration of AMP (0.0325–256 μg mL^{-1}); (b) enlarge view of response study; (c) Calibration curve of BSA/anti-AMP/APTES/nMoS$_2$/ITO immunoelectrode between peak current and concentration of AMP; and (d) Hens-Wolf plot for BSA/anti-AMP/APTES/nMoS$_2$/ITO immunoelectrode.

$$\mathrm{Ipc}_{(BSA/anti-AMP/\mathrm{APTES/nMoS2/ITO})} = -\left[35.68\,\mu\mathrm{A(s/mV)} \times (\text{scan rate[mV/s]})^{1/2}\right] - 82.19\,\mu\mathrm{A},\ \mathrm{R}^2 = 0.991 \tag{8}$$

$$\mathrm{Ipa}_{(BSA/anti-AMP/\mathrm{APTES/nMoS2/ITO})} = \left[48.42\,\mu\mathrm{A(s/mV)} \times (\text{scan rate[mV/s]})^{1/2}\right] - 46.45\,\mu\mathrm{A},\ \mathrm{R}^2 = 0.996 \tag{9}$$

It was seen that an increase in scan rate causes the anodic and cathodic peaks current to move towards the higher and lower potential, respectively. Linearity has been obtained between the difference in magnitude of the anodic and cathodic peak potential vs. square root of scan rate (ΔE = Epa - Epc, where Epa and Epc are anodic and cathodic peak potential, respectively), indicating amiable charge transfer kinetics between electrode and electrolyte as given in Eq. (10) and (11). The scan rate analysis of both BSA/anti-AMP/APTES/MoS$_2$/ITO immunoelectrode and APTES/MoS$_2$/ITO electrode depicts that the oxidation current had moved more towards the positive potential, and similarly, the peak of reduction current has also moved towards the negative potential. Also, the increase in peak potential (E_{pa} and E_{pc}) with a rise in scan rate recommends a slow movement of electrons across the interface [Figs. S7 and S8 (lower inset)] (Lakshmi, Yadav, Mehlawat, Jalandra, Solanki, & Kumar, 2021).

$$\Delta\mathrm{Ep(V)}_{(BSA/anti-AMP/\mathrm{APTES/nMoS2/ITO})} = \left[0.020\,\mathrm{V(s/mV)} \times (\text{scan rate[mV/s]})^{1/2}\right] + 0.080\,\mathrm{V},\ \mathrm{R}^2 = 0.998 \tag{10}$$

$$\Delta\mathrm{Ep(V)}_{(BSA/anti-AMP/\mathrm{APTES/nMoS2/ITO})} = \left[0.020\,\mathrm{V(s/mV)} \times (\text{scan rate[mV/s]})^{1/2}\right] + 0.080\,\mathrm{V},\ \mathrm{R}^2 = 0.998 \tag{11}$$

The kinetic interface factor, for example, standard heterogeneous electron transfer rate constant (K_s), effective surface area (A_e), the surface concentration of redox species (I*), and diffusion constant (D) of BSA/anti-AMP/APTES/MoS$_2$/ITO immunoelectrode and APTES/MoS$_2$/ITO electrode were calculated to investigate electron movements. (detailed information has been explained in Supplementary File). The calculated interface kinetic parameters corresponding to both electrodes has been given in Table S2.

4.4. Electrochemical response analysis of AMP using BSA/anti-AMP/APTES/nMoS$_2$/ITO immunoelectrode

To study the electrochemical behavior between developed BSA/anti-AMP/APTES/nMoS$_2$/ITO immunosensor and AMP concentration, the DPV technique has been conducted. The sensing measurements were repeated thrice. It was seen that with a rise in AMP concentration, the

DPV current decreases because of the anti-AMP-AMP complex formation, i.e., occurring between anti-AMP and AMP, as shown in Fig. 4(a). Moreover, the development of an electrically insulating anti-AMP-AMP complex is responsible for a decrease in current as it restricts the transfer of electrons between $[Fe(CN)_6]^{3-/4-}$ and immunoelectrode (Gupta, Khan, & Solanki, 2016; Kumar, Kumar, et al., 2016). Fig. 4 (b) showed the zoom portion of the electrochemical response study.

Under optimized assay conditions, the calibration curve between the different concentration of AMP and BSA/anti-AMP/APTES/$nMoS_2$/ITO immunoelectrode [Fig. 4 (c)] shows a linear range in the concentration of 0.0325 to 64 μg mL^{-1} after which the saturation of current occurs at higher concentrations with a linear regression coefficient of 0.999. The sensitivity was determined *via* slope of the curve of the proposed immunoelectrode and found to be [41.81 μA (log μg $mL^{-1})^{-1}$] with 0.028 μg mL^{-1} limits of detection (LOD) that was estimated using the standard equation.

$$\text{Limit of detection} = 3\sigma/\text{sensitivity} \quad (12)$$

where σ depicts the standard deviation of the BSA/anti-AMP/APTES/$nMoS_2$/ITO immunosensor.

The association constant (K_a) value was calculated from the Hens-Wolf plot, which is a plot between AMP concentration and AMP concentration/current] for BSA/anti-AMP/APTES/$nMoS_2$/ITO immunoelectrode as given in Fig. 4 (d) and obtained as 74.63 μg mL^{-1}. K_a relies on various conditions of the designed immunosensor, such as the binding sites of biomolecules and how antibodies (anti-AMP) are immobilized on the electrode surface, which could cause various conformation changes in antibody structure on the surface of the electrode. Here, the enhanced value of K_a depicts the rise in the affinity of BSA/anti-AMP/APTES/$nMoS_2$/ITO immunoelectrode towards AMP due to constructive anti-AMP conformation and higher loading on the electrode surface. The value of dissociation constant (K_d) was determined to be 0.358 μg mL^{-1}, signifying a robust, specific affinity for AMP. The K_a value was calculated from the inverse of slope values obtained by the Hanes-Wolf plot's linear fitting, while the K_d value is the product of K_a and the intercept.

4.5. Control, Specificity, Reproducibility, and repeatability of immunoassay

The control experiment was done to examine the electrochemical current response of APTES/$nMoS_2$/ITO electrode with varying concentrations of AMP [Fig. 5 (a)]. All the parameters were kept similar as the electrochemical response studies for BSA/anti-AMP/APTES/$nMoS_2$/ITO immunoelectrode except the immobilization of anti-AMP. The Figure shows no change in DPV current of APTES/$nMoS_2$/ITO electrode on adding a higher concentration of AMP, which might be due to no interaction taking place between APTES/$nMoS_2$/ITO electrode and AMP leading to no change in electrochemical response. Thus, the change in current in response studies is primarily due to the interaction between AMP and anti-AMP and not because of APTES/$nMoS_2$/ITO electrode.

As we know food samples are saturated with a huge amount of inorganic and organic analytes like BSA [100 μM], glucose [100 μM], Vit-C [100 μM], cholesterol [100 μM], norfloxacin [5 mM], ofloxacin [5 mM], ciprofloxacin [5 mM], Na^+ [0.6 g/100 mL], Mg^{++} [0.01 g/mL] etc. The above interferents were made according to their respective concentration in milk and environmental samples. Further, for checking the cross-reactivity of the BSA/anti-AMP/APTES/$nMoS_2$/ITO immunosensor, the sensor response towards Ag-AMP was determined in the presence of various potential interferents in milk and environmental samples [Fig. 5(b)]. Initially, the fabricated BSA/anti-AMP/APTES/$nMoS_2$/ITO immunoelectrode was studied in a fixed concentration of Ag-AMP (8 μg mL^{-1}). Then, gradually different AMP (10 μL) was added every time to the electrolyte premixed with Ag-AMP (8 μg mL^{-1}), and the current response was recorded after the incubation time of 25 min. It was illustrated that the current of all interferents mixed with Ag-AMP

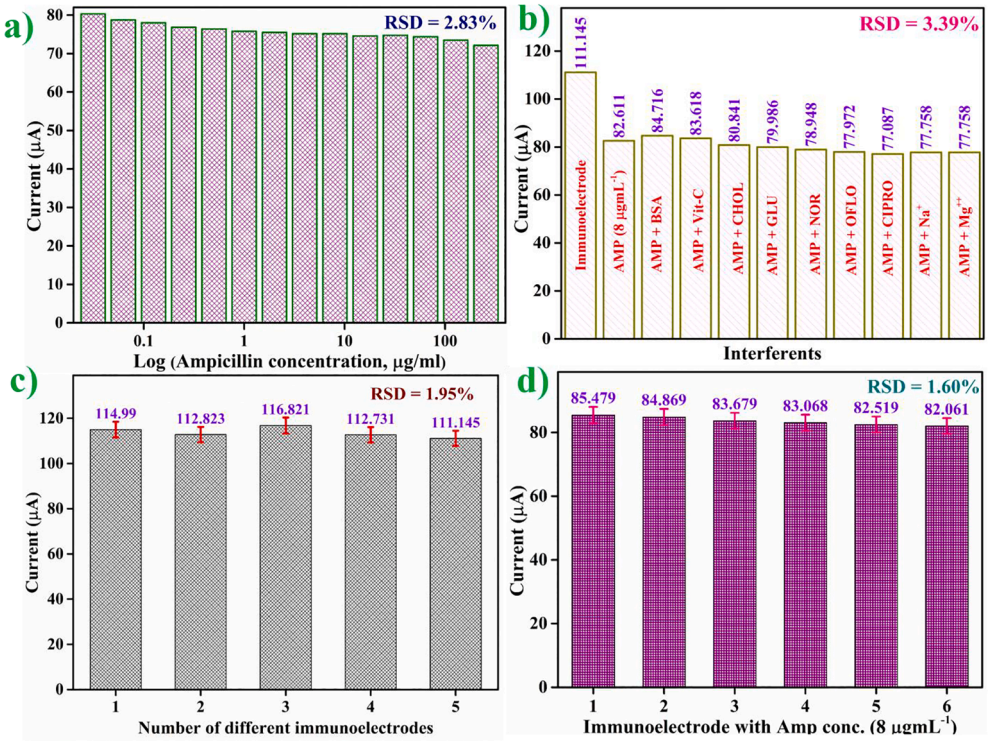

Fig. 5. (a) Control study of APTES/$nMoS_2$/ITO versus AMP concentration (0.0325–256 μg mL^{-1}); (b) Selectivity analysis of BSA/anti-AMP/APTES/$nMoS_2$/ITO immunoelectrode; (c) Reproducibility study for BSA/anti-AMP/APTES/$nMoS_2$/ITO immunoelectrode prepared under similar condition; and (d) Repeatability study of BSA/anti-AMP/APTES/$nMoS_2$/ITO immunoelectrode.

was almost unchanged with an RSD of 3.39%, which indicates good specificity of the biosensor towards Ag-AMP.

The co-efficient of selectivity was calculated as 1 for each interferents using equation.

$$SC = Ic + i/Ic \quad (13)$$

Where, Ic + i and Ic are the values of the current of immunosensor in the presence and absence of interferents, respectively showing negligible variation in the response.

For investigating the reproducibility of BSA/anti-AMP/APTES/$nMoS_2$/ITO immunoelectrode, five different bioelectrodes were taken and used separately for each study using the DPV technique in a similar set of conditions [Fig. 5 (c)]. Likewise, repeatability of the BSA/anti-AMP/APTES/$nMoS_2$/ITO immunoelectrode was performed by taking six consecutive measurements for a particular AMP concentration (8 μg mL^{-1}) using the DPV technique [Fig. 5(d)]. The RSD values for reproducibility and repeatability were found to be in the acceptable range, i.e., 1.95% and 1.60%, respectively.

4.6. Regeneration and stability of immunosensor

Regeneration is a vital factor in fabrication of cost-effective biosensor i.e. reusing the biosensor for many times through a regeneration step. For evaluating the regeneration of BSA/anti-AMP/APTES/$nMoS_2$/ITO immunosensor, the biosensor was investigated after the interactions between AMP and anti-AMP. For this, various types of regeneration solutions were made; HCl (acidic) orglycine-HCl buffer, NaOH (basic), and $MgCl_2$ (salt). In this experiment, 10% DMSO/ formamide (1:1) and 0.010% Tween-20 in PBS (0.2 M) of pH 7.0 were utilized to break the Ab − Ag immune-complex (Sangili, Kalyani, Chen, Nanda, & Jana, 2020). After that, particular concentration of AMP was re-measured by using regenerated BSA/anti-AMP/APTES/$nMoS_2$/ITO immunoelectrode. This study was conducted using a particular concentration of AMP,i.e.,16 μg mL^{-1} to measure the DPV signal, and 30 min was given the time of treatment [Fig. S9 (a)]. The red bar showed the regenerated BSA/anti-AMP/APTES/$nMoS_2$/ITO immunoelectrode i.e. after breakage of specific interaction between AMP and anti-AMP and yellow bar displayed the re-measurement of AMP (16 μg mL^{-1}) with regenerated BSA/anti-AMP/APTES/$nMoS_2$/ITO immunoelectrode.

The variations in peak currents were displayed after six cycles having an RSD value of 1.89%.

The shelf-life of immunoelectrode was determined for 10 weeks at an interval of 1 week *via* the DPV technique. As shown in Fig. S9 (b), the immunoelectrode retains 94% of the peak current till the 8th week. Afterward, a rapid decrease in current was observed, which suggests that the biosensor has good stability up to 8 weeks. 4 °C has been used to store the fabricated BSA/anti-AMP/APTES/$nMoS_2$/ITO immunoelectrode when not in use.

4.7. Application of proposed BSA/anti-AMP/APTES/$nMoS_2$/ITO immunosensor in spiked samples

To prove this method, a test was conducted in real samples to detect AMP. For this test, the real samples such as treated milk, orange juice, and tap water were applied to the surface of fabricated BSA/anti-AMP/APTES/MoS_2/ITO immunoelectrode. The obtained recoveries for AMP and their RSD values from milk, orange juice, and tap water samples are 97.41–102.73%, 96.36–101.44%, and 95.87–100.5%; and 1.91, 2.62, and 3%, respectively, as described in Table S3. These measured values were in good agreement with the data approving the biosensor's reliability and accuracy for its application in real samples.

The given fabricated BSA/anti-AMP/APTES/$nMoS_2$/ITO immunosensor has been compared with the previously reported electrochemical sensors and biosensors to detect AMP (Injac, Kočevar, & Štrukelj, 2009; Karaseva, Ermolaeva, & Mizaikoff, 2016; Khan, Mohd, Bano, Siddiqi, & Asiri, 2015; Mishra, Pulidindi, Kabha, & Gedanken, 2016; Mohamed, 2001; Xu, Wang, & Xiao, 2004) (Table1). From this table, it can be seen that the proposed immunoelectrode has exhibited higher specificity and enhanced detection limit of 0.0325 μg mL^{-1} in comparison to previous sensors and biosensors. To the best of our knowledge, this is the first report on electrochemical biosensors based on anti-AMP for AMP detection with a concentration as low as 0.0325 μg mL^{-1} having high sensitivity of [41.81 μA (log μg mL^{-1})$^{-1}$] and a linear detection range from 0.0325 to 64 μg mL^{-1}.

Table 1
Comparison of BSA/anti-AMP/APTES/$nMoS_2$/ITOimmunoelectrode with earlier reported AMP detection methods.

Method	Sensing technique	Linear range (μgmL^{-1})	LOD (μgmL^{-1})	Ref.
Spectrophotometry	Absorbance	1.5–77.5	0.5	(Mohamed, 2001)
Spectrophotometry	Absorbance	5–30	0.162	(Khan, Mohd, Bano, Siddiqi, & Asiri, 2015)
Spectrophotometry	Absorbance	50–260	0.866	(Khan, Mohd, Bano, Siddiqi, & Asiri, 2015)
Spectrophotometry	Absorbance	2–80	1.5	(Xu, Wang, & Xiao, 2004)
HPLC	Absorbance	10–100	3.0	(Injac, Kočevar, & Štrukelj, 2009)
Capillary electrophoresis (MEKC)	Absorbance	3–265	0.6	(Injac, Kočevar, & Štrukelj, 2009)
Piezoelectric sensors	MIP	0.10–1.0	0.09	(Karaseva, Ermolaeva, & Mizaikoff, 2016)
Optical sensor	Absorbance	6.6–200	6.6	(Mishra, Pulidindi, Kabha, & Gedanken, 2016)
Electrochemical immunosensor	DPV	0.0325–64	0.028	Present work

5. Conclusions

The fabrication of BSA/anti-AMP/$nMoS_2$/ITO immunoelectrode has been successfully implemented to develop an AMP biosensor. The synthesis of $nMoS_2$ NPs was carried out *via* a low-temperature, one-step hydrothermal process characterized through XRD, FTIR, and TEM. The thin films of APTES/$nMoS_2$/ITO were electrophoretically deposited on ITO coated glass that was further utilized to immobilize anti-AMP by EDC-NHS coupling. The blocking agent BSA was used for covering the non-specific sites for the electrochemical AMP detection. The FE-SEM was used to examine the morphological changes of developed electrodes, where as the properties of the oxidation/reduction of BSA/anti-AMP/$nMoS_2$/ITO immunoelectrode were completed utilizing the CV technique. The response of BSA/anti-AMP/$nMoS_2$/ITO immunoelectrode concerning different AMP concentrations (0.0325–262 μg mL^{-1}) was done with the DPV technique. The results of immunoelectrode showed outstanding linearity in the range, 0.0325–64 μg mL^{-1} (with R^2

= 0.999) with AMP concentration, high sensitivity [41.81 μA (log μg $mL^{-1})^{-1}$], and lower detection limit of 0.028 μg mL^{-1}as compared to previously reported biosensors. The proposed immunoelectrode showed high specificity to AMP and was applied as a sensing platform to study the real samples in spiked samples of milk, orange juice, and tap water with excellent results. The outcomes of the fabricated electrode showed superior performance in terms of lower detection limit, linear range, and sensitivity compared to earlier developed biosensors. The BSA/anti-AMP/nMoS_2/ITO immunoelectrode presented an innovative approach for developing fast, biocompatible, and highly sensitive biosensors and biochip devices.

Author contribution

Conceptualization: A.K.Y; Experimental investigation: A.K.Y and D. V.; Writing-original draft preparation: A.K.Y and D.V.; Writing-review and editing: G.B.V.S.L, S.E., and P.R.S.; Resources: P.R.S.; Supervision: P.R.S.

CRediT authorship contribution statement

Amit K. Yadav: Conceptualization, Data curation, Investigation, Methodology, Validation, Writing - original draft. **Damini Verma:** Data curation, Formal analysis, Investigation, Validation, Writing - original draft. **G.B.V.S. Lakshmi:** Formal analysis, Software, Visualization, Writing - original draft, Writing - review & editing. **Sergei Eremin:** Formal analysis, Supervision, Visualization, Writing - review & editing. **Pratima R. Solanki:** Funding acquisition, Project administration, Resources, Supervision, Software, Writing - review & editing.

Declaration of Competing Interest

The authors declare that they have no known competing financial interests or personal relationships that could have appeared to influence the work reported in this paper.

Acknowledgment

All the authors greatly acknowledge AIRF, JNU for providing the facilities for characterization. We are also grateful to the Government of India from Indo-Russia (DBT/IC-2/Indo-Russia/2017-19/02), ICMR, and DST-BDTD project that has financially supported the present work. GBVSL is thankful to DST, India for funding through Women Scientist project.

Appendix A. Supplementary data

Supplementary data to this article can be found online at https://doi.org/10.1016/j.foodchem.2021.130245.

References

Cai, S., & Singh, B. R. (2004). A distinct utility of the amide III infrared band for secondary structure estimation of aqueous protein solutions using partial least squares methods. *Biochemistry, 43*(9), 2541–2549.

Cardoso, A. R., Tavares, A. P. M., & Sales, M. G. F. (2018). In-situ generated molecularly imprinted material for chloramphenicol electrochemical sensing in waters down to the nanomolar level. *Sensors and Actuators B: Chemical, 256*, 420–428.

Feng, C., Ma, J., Li, H., Zeng, R., Guo, Z., & Liu, H. (2009). Synthesis of molybdenum disulfide (MoS2) for lithium ion battery applications. *Materials Research Bulletin, 44*(9), 1811–1815.

Fowler, J. M., Wong, D. K., Halsall, H. B., & Heineman, W. R. (2008). Recent developments in electrochemical immunoassays and immunosensors. In *Electrochemical sensors, biosensors and their biomedical applications* (pp. 115–143). Academic Press.

Geng, D.i., Bo, X., & Guo, L. (2017). Ni-doped molybdenum disulfide nanoparticles anchored on reduced graphene oxide as novel electroactive material for a non-enzymatic glucose sensor. *Sensors and Actuators B: Chemical, 244*, 131–141.

Gupta, P. K., Khan, Z. H., & Solanki, P. R. (2016). One-step electrodeposited porous ZnO thin film based immunosensor for detection of Vibrio cholerae toxin. *Journal of The Electrochemical Society, 163*(7), B309–B318.

Hall, W. (2018). Superbugs: An arms race against bacteria: Harvard University Press.

Huang, J., He, Y., Jin, J., Li, Y., Dong, Z., & Li, R. (2014). A novel glucose sensor based on MoS_2 nanosheet functionalized with Ni nanoparticles. *Electrochimica Acta, 136*, 41–46.

Injac, R., Kočevar, N., & Štrukelj, B. (2009). Optimized method for determination of amoxicillin, ampicillin, sulfamethoxazole, and sulfacetamide in animal feed by micellar electrokinetic capillary chromatography and comparison with high-performance liquid chromatography. *Croatica Chemica Acta, 82*(3), 685–694.

Jamieson, O., Soares, T. C. C., de Faria, B. A., Hudson, A., Mecozzi, F., Rowley-Neale, S. J., … Crapnell, R. D. (2020). Screen printed electrode based detection systems for the antibiotic amoxicillin in aqueous samples utilising molecularly imprinted polymers as synthetic receptors. *Chemosensors, 8*(1), 5. https://doi.org/10.3390/chemosensors8010005.

Karaseva, N., Ermolaeva, T., & Mizaikoff, B. (2016). Piezoelectric sensors using molecularly imprinted nanospheres for the detection of antibiotics. *Sensors and Actuators B: Chemical, 225*, 199–208.

Khan, A. A. P., Mohd, A., Bano, S., Siddiqi, K. S., & Asiri, A. M. (2015). Spectrophotometric methods for the determination of ampicillin by potassium permanganate and 1-chloro-2, 4-dinitrobenzene in pharmaceutical preparations. *Arabian Journal of Chemistry, 8*(2), 255–263.

Kim, S. J., Mondal, S., Min, B. K., & Choi, C.-G. (2018). Highly sensitive and flexible strain–pressure sensors with cracked paddy-shaped MoS_2/graphene foam/Ecoflex hybrid nanostructures. *ACS Applied Materials & Interfaces, 10*(42), 36377–36384.

Kumar, S., Kumar, S., Tiwari, S., Augustine, S., Srivastava, S., Yadav, B. K., & Malhotra, B. D. (2016). Highly sensitive protein functionalized nanostructured hafnium oxide based biosensing platform for non-invasive oral cancer detection. *Sensors and Actuators B: Chemical, 235*, 1–10.

Kumar, S., Sharma, J. G., Maji, S., & Malhotra, B. D. (2016). Nanostructured zirconia decorated reduced graphene oxide based efficient biosensing platform for non-invasive oral cancer detection. *Biosensors and Bioelectronics, 78*, 497–504.

Lakshmi, G. B. V. S., Yadav, A. K., Mehlawat, N., Jalandra, R., Solanki, P. R., & Kumar, A. (2021). Gut microbiota derived trimethylamine N-oxide (TMAO) detection through molecularly imprinted polymer based sensor. *Scientific reports, 11*(1), 1338. https://doi.org/10.1038/s41598-020-80122-6.

Lee, C., Yan, H., Brus, L. E., Heinz, T. F., Hone, J., & Ryu, S. (2010). Anomalous lattice vibrations of single-and few-layer MoS_2. *ACS Nano, 4*(5), 2695–2700.

Michael, C. A., Dominey-Howes, D., & Labbate, M. (2014). The antimicrobial resistance crisis: Causes, consequences, and management. *Frontiers in public health, 2*, 145.

Mishra, R. K., Pulidindi, I. N., Kabha, E., & Gedanken, A. (2016). In situ formation of carbon dots aids ampicillin sensing. *Analytical Methods, 8*(11), 2441–2447.

Mohamed, G. G. (2001). Spectrophotometric determination of ampicillin, dicluxacillin, flucloxacillin and amoxicillin antibiotic drugs: Ion-pair formation with molybdenum and thiocyanate. *Journal of Pharmaceutical and Biomedical Analysis, 24*(4), 561–567.

Pavia, D. L., Lampman, G. M., Kriz, G. S., & Vyvyan, J. A. (2014). *Introduction to spectroscopy*. Nelson Education.

Pourabbas, B., & Jamshidi, B. (2008). Preparation of MoS_2 nanoparticles by a modified hydrothermal method and the photo-catalytic activity of MoS_2/TiO_2 hybrids in photo-oxidation of phenol. *Chemical Engineering Journal, 138*(1-3), 55–62.

Pua, F. L., Chia, C. H., Zakari, S., Liew, T. K., Yarmo, M. A., & Huang, N. M. (2010). Preparation of transition metal sulfide nanoparticles via hydrothermal route. *Sains Malaysiana, 39*(2), 243–248.

Sangili, A., Kalyani, T., Chen, S.-M., Nanda, A., & Jana, S. K. (2020). Label-free electrochemical immunosensor based on one-step electrochemical deposition of AuNP-RGO nanocomposites for detection of endometriosis marker CA 125. *ACS Applied Bio Materials, 3*(11), 7620–7630.

Shin, M., Yoon, J., Yi, C., Lee, T., & Choi, J. W. (2019). Flexible HIV-1 biosensor based on the Au/MoS_2 nanoparticles/Au nanolayer on the PET substrate. *Nanomaterials, 9*(8), 1076.

Singhal, C., Khanuja, M., Chaudhary, N., Pundir, C., & Narang, J. (2018). Detection of chikungunya virus DNA using two-dimensional MoS_2 nanosheets based disposable biosensor. *Scientific Reports, 8*(1), 1–11.

Solé, S., Merkoci, A., & Alegret, S. (2001). New materials for electrochemical sensing III. Beads. *TrAC Trends in Analytical Chemistry, 20*(2), 102–110.

Srivastava, S., Kumar, V., Ali, M. A., Solanki, P. R., Srivastava, A., Sumana, G., … Malhotra, B. D. (2013). Electrophoretically deposited reduced graphene oxide platform for food toxin detection. *Nanoscale, 5*(7), 3043. https://doi.org/10.1039/c3nr32242d.

Syska, J. (2013). Frieden wave-function representations via an Einstein-Podolsky-Rosen-Bohm experiment. *Physical Review E, 88*(3), Article 032130.

Tiwari, S., Gupta, P. K., Bagbi, Y., Sarkar, T., & Solanki, P. R. (2017). L-cysteine capped lanthanum hydroxide nanostructures for non-invasive detection of oral cancer biomarker. *Biosensors and Bioelectronics, 89*, 1042–1052.

Wang, G., Wang, Z., Zhang, Y., Fei, G., & Zhang, L. (2004). Controlled synthesis and characterization of large-scale, uniform $Dy(OH)_3$ and Dy_2O_3 single-crystal nanorods by a hydrothermal method. *Nanotechnology, 15*(9), 1307–1311.

Wang, T., Yin, H., Zhang, Y., Wang, L., Du, Y., Zhuge, Y., & Ai, S. (2019). Electrochemical aptasensor for ampicillin detection based on the protective effect of aptamer-antibiotic conjugate towards DpnII and Exo III digestion. *Talanta, 197*, 42–48.

Wang, T., Zhu, H., Zhuo, J., Zhu, Z., Papakonstantinou, P., Lubarsky, G., … Li, M. (2013). Biosensor based on ultrasmall MoS2 nanoparticles for electrochemical detection of H_2O_2 released by cells at the nanomolar level. *Analytical Chemistry, 85*(21), 10289–10295.

Xu, L., Wang, H., & Xiao, Y. (2004). Spectrophotometric determination of ampicillin sodium in pharmaceutical products using sodium 1, 2-naphthoquinone-4-sulfonic as the chromogentic reagent. *Spectrochimica Acta Part A: Molecular and Biomolecular Spectroscopy, 60*(13), 3007–3012.

Yadav, A. K., Dhiman, T. K., Lakshmi, G. B. V. S., Berlina, A. N., & Solanki, P. R. (2020). A highly sensitive label-free amperometric biosensor for norfloxacin detection based on chitosan-yttria nanocomposite. *International Journal of Biological Macromolecules, 151*, 566–575.

Yan, L., Shi, H., Sui, X., Deng, Z., & Gao, L.i. (2017). MoS_2-DNA and MoS_2 based sensors. *RSC Advances, 7*(38), 23573–23582.

Yuan, R., Yan, Z., Shaga, A., & He, H. (2021). Design and fabrication of an electrochemical sensing platform based on a porous organic polymer for ultrasensitive ampicillin detection. *Sensors and Actuators B: Chemical, 327*, Article 128949.

Zhang, W., Zhang, P., Su, Z., & Wei, G. (2015). Synthesis and sensor applications of MoS_2-based nanocomposites. *Nanoscale, 7*(44), 18364–18378.

Zhou, M., Lou, X. W.(., & Xie, Y.i. (2013). Two-dimensional nanosheets for photoelectrochemical water splitting: Possibilities and opportunities. *Nano Today, 8*(6), 598–618.

Zhu, C., Zeng, Z., Li, H., Li, F., Fan, C., & Zhang, H. (2013). Single-layer MoS_2-based nanoprobes for homogeneous detection of biomolecules. *Journal of the American Chemical Society, 135*(16), 5998–6001.